metals

MDPI

Article

Characterization of Hot Deformation Behavior and Processing Maps Based on Murty Criterion of SAE8620RH Gear Steel

Songjun Chen [1,2], Liejun Li [1] and Ruxue Zhu [2,*]

[1] Guangdong Provincial Key Laboratory for Processing and Forming of Advanced Metallic Materials, South China University of Technology, Guangzhou 510640, China; jasonchensj@163.com (S.C.); liliejun@scut.edu.cn (L.L.)
[2] Shaoneng Group Shaoguan Hongda Gear Co., Ltd., Shaoguan 512029, China
* Correspondence: xueruzhusc@163.com

Abstract: The hot deformation behavior and microstructure evolution of the SAE8620RH gear steel were investigated through a single-pass hot compression test at deformation temperatures between 850 and 1100 °C and strain rates between 0.02 and 8.0 s^{-1} by 60% reduction. A novel strain compensation constitutive model was developed, and the 2D processing maps were established by Murty's criterion. Results showed that the relationship between material-related parameters and strain can be mathematically expressed by a highly reliable 8th-order polynomial. The constructed strain compensation constitutive model demonstrated remarkable predictive precision, as evidenced by the correlation coefficient (R) and the absolute values of average relative error (AARE) of 0.978 and 4%, respectively. The flow instability domains considerably expanded towards the high deformation temperature region as the strain increased. Microstructure analysis confirmed the accuracy of the processing map constructed by Murty's criterion. The most noticeable optimum processing windows for SAE8620RH gear steel at a strain of 0.7 occurred within the temperature range of 1000–1100 °C and the strain rate range of 0.3–1.0 s^{-1}, due to high η values exceeding 0.3 and equiaxial dynamic recrystallization microstructure.

Keywords: hot deformation; strain compensation constitutive model; power dissipation map; instability parameter; processing map; Murty's criterion

check for updates

Citation: Chen, S.; Li, L.; Zhu, R. Characterization of Hot Deformation Behavior and Processing Maps Based on Murty Criterion of SAE8620RH Gear Steel. *Metals* **2023**, *13*, 1832. https://doi.org/10.3390/met13111832

Academic Editor: Mohammad Jahazi

Received: 22 September 2023
Revised: 19 October 2023
Accepted: 27 October 2023
Published: 31 October 2023

Copyright: © 2023 by the authors. Licensee MDPI, Basel, Switzerland. This article is an open access article distributed under the terms and conditions of the Creative Commons Attribution (CC BY) license (https://creativecommons.org/licenses/by/4.0/).

1. Introduction

SAE8260RH gear steel is extensively employed in industries characterized by stringent material performance criteria, such as automotive, maritime, and mechanical engineering, owing to its remarkable attributes of elevated purity, exceptional hardenability, and prolonged fatigue endurance [1]. The successful application of SAE8260RH gear steel necessitates adequate core hardenability, favorable carburizing layer hardenability, a superior banded structure, and minimal nonmetallic inclusions [2]. Obviously, a significant amount of investigation has been directed towards the optimization of carburizing and quenching processes, as well as the control of inclusions [3–5]. In fact, during the manufacturing process, gear steel undergoes a complex thermal deformation condition to attain a uniform and refined structure. This structural characteristic is also crucial in achieving exceptional performance and dimensional stability. Nonetheless, if the thermal deformation parameters are not appropriately selected, the formation of defects, such as localized deformation, adiabatic shear bands, and wedge cracks may occur [6,7]. Dynamic recrystallization has the potential to eliminate deformation-induced defects and decrease the average grain size, which plays a crucial role in determining the microstructure and mechanical properties [8]. There are fewer studies on the hot deformation behavior of SAE8260RH gear steel at high temperatures. Therefore, there is a need to study the thermal deformation mechanism and the microstructural evolution of SAE8620RH gear steeds.

The hot deformation behavior of metals was affected strongly by deformation parameters, such as deformation temperature, strain rate, and strain, as well as by the characteristics of secondary phases [9–11]. Chen conducted a study on the thermal deformation behavior of 17Cr2Ni2MoVNb and 20Cr2Ni4A gear steels, revealing that both caused dynamic recrystallization at low strain rates and high deformation temperatures [12]. Notably, the presence of Mo and Nb elements in varying proportions resulted in higher stress and critical stress deformation activation energy for 17Cr2Ni2MoVNb steel compared to 20Cr2Ni4A gear steels. In addition, the thermal deformation constitutive equation serves as a mathematical representation for simulating the rheological behavior of materials, enabling the characterization of the intricate nonlinear correlation between flow stress and thermal deformation parameters [13]. Nevertheless, the determination of a rational constitutive relationship to describe flow stress is challenging due to the multitude of factors influencing it [14]. The most extensively employed is the Arrhenius constitutive mode [15–17].

However, the Arrhenius constitutive mode is only a flow stress equation related to deformation temperature and strain rate without considering the factor of strain. The material-dependent constants and activation energy are affected by strains [18]. This is evident in the notable disparity in flow stress requirements for steel when subjected to 10% and 80% deformation. Consequently, efforts were made to describe the relationship between flow stress and strain more comprehensively. With the aim of enhancing the accuracy of the constitutive equation, the strain parameter is incorporated into the Arrhenius constitutive model. Wang et al. established six constitutive equations to study the deformation behavior of powder metallurgy pure tungsten at deformation temperatures from 1523 K to 1823 K and strain rates from 0.001 to 1.0 s^{-1} [19]. The findings revealed that the Arrhenius model with strain compensation exhibited the highest accuracy due to its consideration of the combined effects of strain, strain rate, and deformation temperature. Correspondingly, the value of the correlation coefficient (R) was 0.9966, and the value of the average absolute relative error (AARE) was 1.7103. Similarly, Chen's investigation into 30Cr4MoNiV UHS steel also indicated that the flow stress can be reliably estimated through the constitutive equation with strain-dependent constants in the temperature range of 1173–1373 K and a strain rate of 0.01–10.0 s^{-1} [20]. This conclusion was supported by the high R value of 0.9906, which closely approximated 1.0. Hence, it is necessary to explore the relationship between strain and material-related constants to establish the relationship between strain and flow stress.

The thermal processing map serves to delineate the flow instability of metal materials under diverse thermal processing parameters, thereby facilitating the determination of appropriate process parameters for practical production. Consequently, controlled rolling enables the attainment of desirable microstructures and exceptional properties in metal materials [21]. The dynamic materials model (DMM) is a commonly utilized physical model in the construction of thermal processing maps [22]. Prasad et al. have employed the DMM model that enables the prediction of thermal processability, microstructural evolution mechanisms, and flow stability across various deformation temperatures and strain rates [23,24]. Within this model, the nonlinearity of the power dissipation efficiency during thermal deformation is taken into account. Subsequently, numerous scholars have put forth various models for instability criteria grounded in this theory and have developed instability maps to forecast flow instability [25–27].

The thermal processing map is an amalgamation of the power dissipation map and the instability map. The construction of the instability map relies on the strain rate sensitivity coefficient, denoted as m. Prasad et al. regarded m as a constant in the equation of power dissipation efficiency [28]. The constancy of the m value is limited to pure metals, as it fluctuates with changes in temperature and strain rates in complex alloys. Murty et al. modified the power dissipation efficiency equation and established a more suitable instability criterion for metal materials [29]. Based on the Prasad criteria, Murty criteria, and Poletti criteria, Shi et al. constructed thermal processing maps for LZ50 steel at strains of 0.35 and 0.88, within a temperature range of 870–1170 °C and a strain rate of

0.01–10 s^{-1} [30]. Their analysis revealed that the processing maps obtained by Murty's criterion exhibited greater accuracy and determined the optimal parameters within the range of medium temperature and medium strain rate, specifically at 1020 °C and 0.5 s^{-1}. Similarly, Zhong et al.'s investigation on the hot deformation characterization of Al-Cu-Li X2A66 alloy demonstrated that Murty's criterion displayed the utmost precision, and the optimized processing parameters were identified as 480–500 °C/0.001–0.1 s^{-1} and 420–480 °C/0.1–1 s^{-1} [31].

Considering the aforementioned findings, it is of great value to investigate the evolution of microstructure and construct processing maps for the SAE8620RH gear steel during the thermal working process, with the aim of optimizing the microstructure and enhancing performance. Consequently, a single-pass hot compression experiment was conducted to investigate its hot deformation behavior. Furthermore, by analyzing the acquired true stress-strain curves and accounting for the influence of strain, precise constitutive equations were formulated to predict the flow stresses. Subsequently, a processing map was developed using Murty's criterion. By integrating the processing map with the microstructure characteristics, potential factors leading to deformation instability were mitigated, and the optimal range of process parameters was determined.

2. Materials and Methods

The experimental material of SAE8620RH gear steel utilized in this study was a 50-mm-diameter bar from a steel mill. The production process of SAE8620RH gear steel was as follows: 60t EAF → LF → VD → LF → CC. Then the square billet with a cross-section of 250 × 280 mm^2 produced by curved billet continuous casting machines was rolled into round bars with diameters of 50 mm. The chemical composition of the test steel's main elements was determined using the QSN750-IIdirect reading spectrometer (OBLF, Dortmund, Germany), and the resulting composition is presented in Table 1. Furthermore, the CS844 infrared carbon sulfur meter (LECO, Saint Joseph, MO, USA) was employed to determine the chemical compositions of the S and C elements in the SAE8620RH gear steel.

Table 1. Chemical composition of the main elements in SAE8620RH gear steel (wt. %).

C	Mn	Si	Cr	Ni	Mo	Al	Ni	S	P
0.22	0.78	0.19	0.53	0.41	0.17	0.027	0.56	0.023	0011

In order to investigate the hot deformation behavior of SAE8620RH gear steel at high temperatures and construct the processing map, single-pass hot compression tests were performed. Cylindrical specimens with dimensions of φ10 × 15 mm for hot compression tests were extracted from the φ50 mm bar using a wire-cutting machine. The hot compression test was performed using a Gleeble-3800 Thermo-Mechanical Simulator, and the specific procedure for the single-pass hot compression test is illustrated in Figure 1.

The specimens underwent a heating process to a temperature of 1150 °C at a rate of 5 °C/s and were maintained for a duration of 3 min in order to achieve complete solidification of the alloying elements within the austenite. Following this, the specimens were cooled to the deformation temperature range of 850–1100 °C at 5 °C/s and held for 10 s, subsequently deformed by 60% reduction with strain rates of 0.02–8.0 s^{-1}. Finally, the deformed specimens were water quenched to room temperature to preserve the prior austenite microstructures. In order to ensure the reproducibility of the experiments, each group of experiments was performed three times.

Before the hot compression test, the specimen was first prepared by polishing both ends with fine sandpaper to ensure a consistent, smooth surface. Additionally, the K-type thermocouple wire was welded to the axial center of the cylindrical specimen to monitor temperature fluctuations throughout the experimental procedure. Following this, a molybdenum disulfide high-temperature lubricant was evenly applied to both ends. Subsequently, circular graphite flakes, with a diameter exceeding that of the cylindrical

specimen by 2 mm, were affixed to both ends. This application aimed to minimize friction between the specimen and the indenter and enhance the deformation stability. Finally, tantalum foils with a thickness of 0.1 mm were placed between the indenters and the ends of the cylindrical specimen with graphite flakes, respectively, to prevent diffusion of the specimen during high-temperature deformation and to bind the indenter interface. The entire compression experiment was conducted in a vacuum state with a vacuum degree of approximately 1.2×10^{-1} torr.

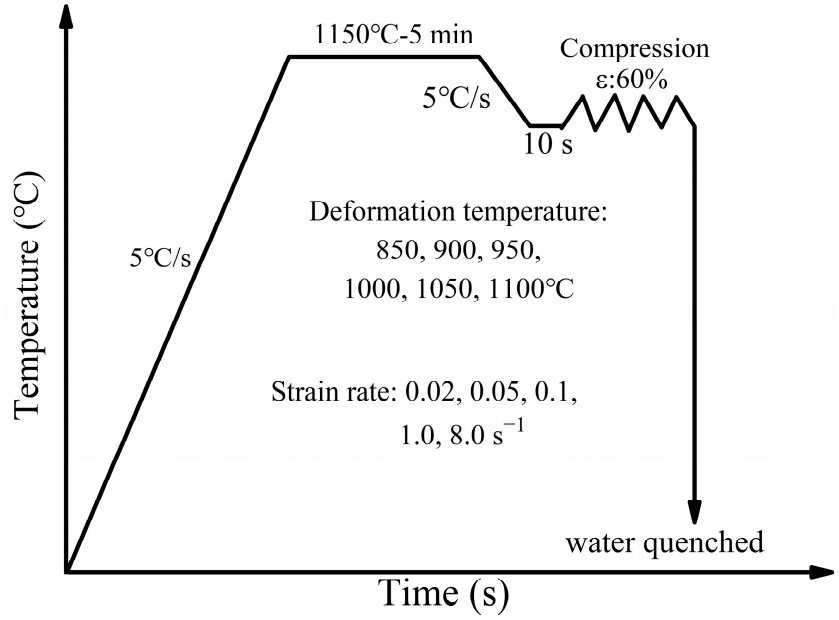


Figure 1. Schematic diagram of single-pass hot compression scheme for the SAE8620RH gear steel.

Based on the force and displacement data collected by Gleeble-3800 Thermo-Mechanical Simulator, the true stresses of the specimen during compression were determined using the principle of volume invariance. The stress-strain data of SAE8620RH gear steel were processed using the Origin8.5 software equipped with the Gleeble-3800 Thermo-Mechanical Simulator. The data for strain compensation constitutive equation and processing maps based on Murty's criterion were processed and calculated using the Matlab 7.0 software. Detailed calculations, equations, and methods can be found in Sections 3.2 and 3.3. Subsequently, these results were imported into the Origin8.5 software for visualization.

The water-quenched specimens were precisely sectioned along the radial direction at the specimen's center using a wire-cutting machine. Following rough grinding, fine grinding, and polishing, the specimens were subjected to corrosion in a saturated picric acid solution with detergent for approximately 3 min. The temperature of the saturated picric acid solution was set within the range of 50–75 °C, depending on the different deformation parameters.

The well-corroded specimens were examined and analyzed using a metallographic microscope of Leica DM4000M to investigate the microstructure evolution. The average size of the prior austenite grains was determined using the intercept method with the free ImageJ2 software.

3. Results and Discussion

3.1. Flow Stress and Microstructure Evolution

Figure 2 illustrates the true stress-strain curves of the SAE8620RH gear steel subjected to a 60% reduction at various strain rates and temperatures. Initially, the true stresses exhibited a substantial increase with increasing strain. However, as the strain continued to increase, the rate of increase in the true stress gradually diminished. Subsequently, the

true stress displayed three distinct trends with increasing strain, attributable to variations in strain rates and deformation temperatures. (I) The flow stress exhibited a peak value as strain increased at low strain rates and high deformation temperatures (0.05–0.1 s^{-1}, T > 950 °C; 1.0–8.0 s^{-1}, T > 1050 °C), followed by a subsequent decrease and eventual attainment of a relatively stable state. The presence of this peak stress suggested the occurrence of dynamic recrystallization of austenite during deformation. Consequently, the deformation mechanism at these parameters can be considered as dynamic recrystallization. (II) The stress did not exhibit a decrease but rather maintained a stable level after reaching its peak (1.0 s^{-1}, T: 900–1000 °C; 8.0 s^{-1}, T: 1050 °C), indicating the establishment of an equilibrium state between the dynamic softening and work hardening effects, which corresponded to a partially dynamically recrystallized austenite grain. (III) The flow stress exhibited a continuous increase with increasing strain without the occurrence of a peak stress, albeit at a gradually decelerated rate (1.0–8.0 s^{-1}, T < 900 °C). This deceleration in stress increment was attributed to the dynamic recovery of the deformed austenite. This type of stress-strain curve is known as the dynamic reversion curve. It should be noted that the work-hardening effect dominates at low temperatures and high strain rates.

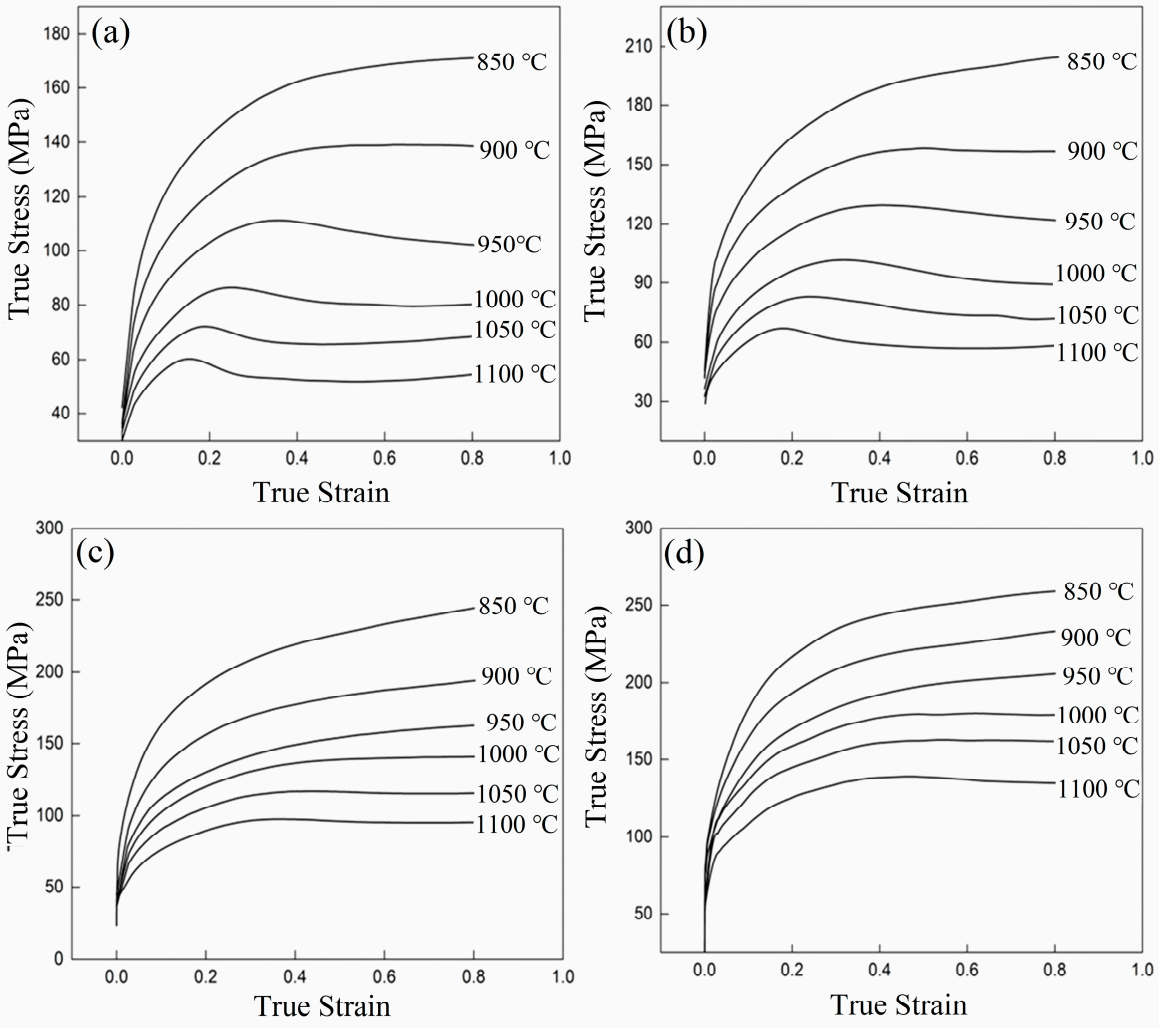


Figure 2. The true stress-strain curves of SAE8620RH gear steel at different strain rates: (**a**) 0.05 s^{-1}; (**b**) 0.1 s^{-1}; (**c**) 1.0 s^{-1}; (**d**) 8.0 s^{-1}.

The alteration in flow stress signified the modifications in the microstructure during thermal deformation, particularly in dislocation density [32]. At an equivalent strain rate, an increase in deformation temperature facilitated the attainment of peak flow stress and

reduced the necessary strain. Consequently, dynamic recrystallization of the deformed austenite was more probable. For instance, when the strain rate was 0.05 s^{-1}, the true strain needed to achieve peak stress decreased from 0.181 to 0.316 as the deformation temperature rose from 1000 °C to 1100 °C. Furthermore, a lower strain rate resulted in a diminished strain requirement for the stress peak (Figure 2b,c). However, the occurrence of dynamic recrystallization of austenite at very slow strain rates was hindered when the temperature was excessively low (Figure 2c,d). It was evident that the three deformation parameters were interconnected and collectively impacted the deformed austenite dynamic recrystallization.

Figure 3 shows the true stress curves of the SAE8620RH gear steel at varying strains. The relationship between deformation temperature and flow stress exhibited an inverse proportionality, as the stress diminished with increasing deformation temperature (Figure 3a,c). During the thermal deformation process, both dynamic recovery and recrystallization were thermally activated processes that involved atomic diffusion. The increase in deformation temperature induced thermal activation of the materials, consequently enhancing the driving force behind the dynamic softening effect. At elevated temperatures, dislocations could easily overcome the solid solution atomic pinning effect, thereby facilitating dynamic reversion and recrystallization through cross-slip and climbing mechanisms. This ultimately led to an augmented nucleation and growth rate of dynamic recrystallization. Furthermore, the influence of deformation temperature on true stress and dynamic recrystallization may also be related to the carbides of Mo or Cr elements in SAE8620RH gear steel. Previous studies have demonstrated that deformation at lower temperatures facilitated austenite strain-induced precipitation, which could hinder dislocation rearrangement and grain boundary migration, consequently impeding the nucleation and growth of recrystallized grains [33]. Zheng et al. studied the hot deformation characteristics of a Fe-Cr-W-Mo-V-C steel, revealing that a decrease in deformation temperature leads to a reduction in the quantity and dimensions of carbides, resulting in a substantial increase in stress and hindering the process of recrystallization [34].

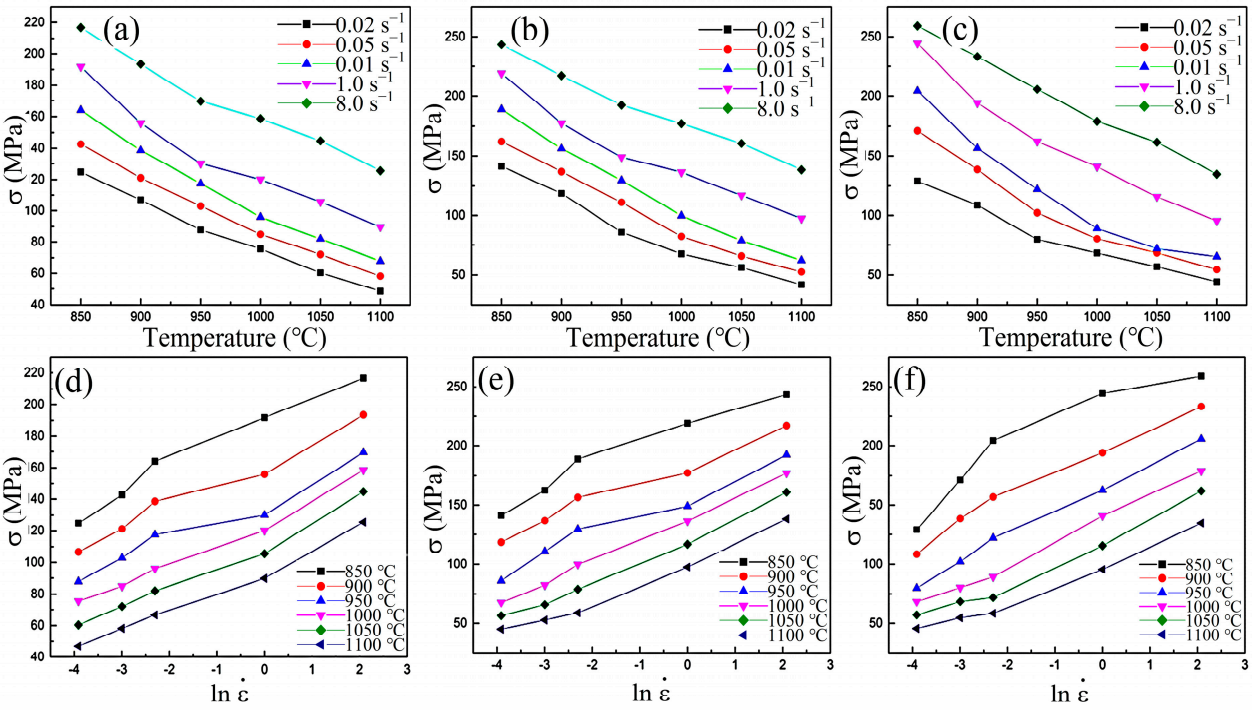


Figure 3. The variation curves of the true stress under different strain: (**a**,**d**) 0.2; (**b**,**e**) 0.4; (**c**,**f**) 0.8.

Consequently, the deformed grains underwent a rapid transformation into isometric, dense, dynamically recrystallized grains, leading to a reduction in flow stress. Contrary

to the temperature effect, the true stress increased with the increase in strain rate. Larger strain rates increased dislocation growth rates, densities, and nucleation points, leading to a significant increase in the hindering effect between dislocations.

The prior austenite grains of SAE8620RH gear steel under various deformation temperatures with a strain rate of 0.1 s^{-1} are shown in Figure 4a,c. At 850 °C, the prior austenite exhibited elongation along the direction of deformation, displaying a pronounced directional characteristic (Figure 4a). Combined with the flow stress curve in Figure 2b, the true stress deformed at 850 °C with 0.1 s^{-1} increased continuously with increasing strain without the peak stress occurrence, showing an obvious work-hardening effect. At a temperature of 1000 °C, the elongated austenite grains completely disappeared and were replaced by equiaxed austenite grains measuring approximately 30.6 μm in size. Upon increasing the deformation temperature to 1100 °C, the equiaxed austenite grains exhibited an average size of approximately 45.3 μm. Furthermore, some coarse austenite grains were also observed, indicating that austenite grains had started to coarsen (Figure 4c).

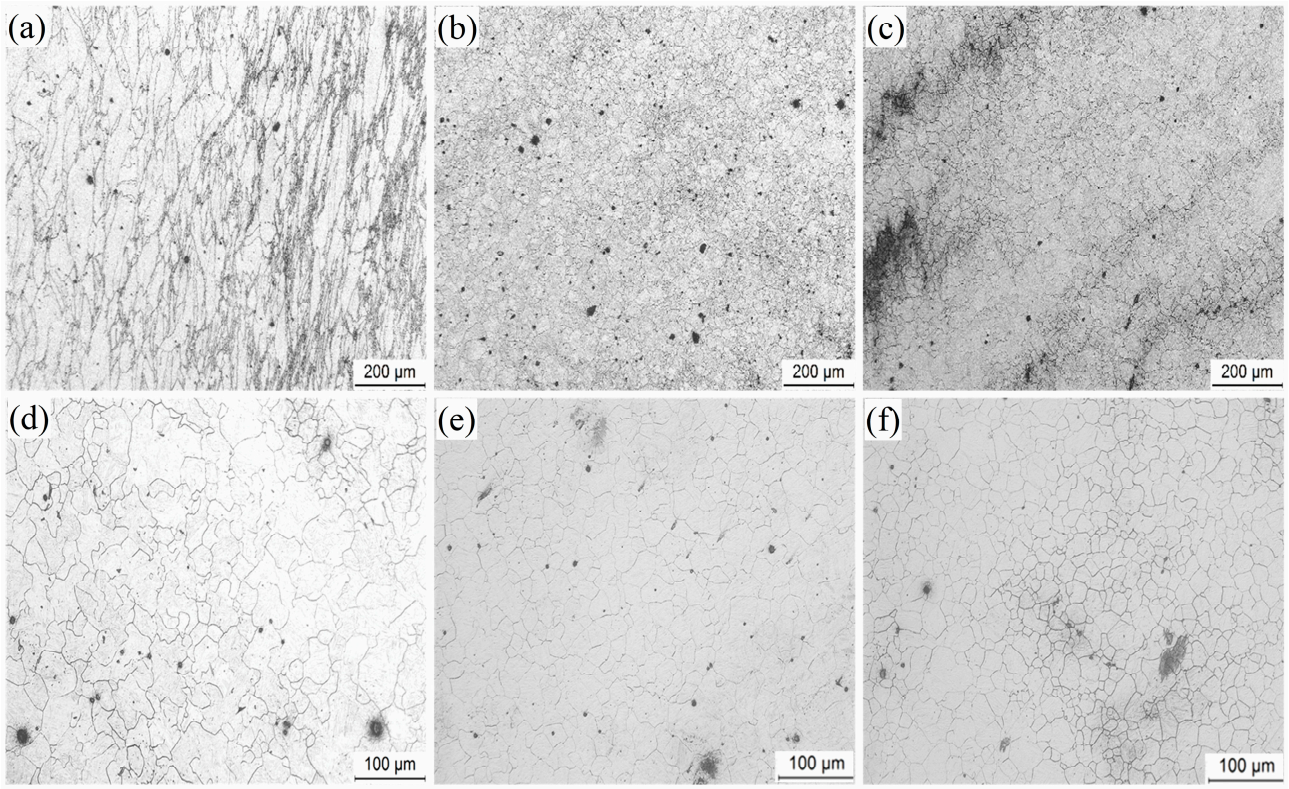


Figure 4. The prior austenite grains of SAE8620RH gear steel under different deformation parameters (**a**) 0.1 s^{-1}-850 °C; (**b**) 0.1 s^{-1}-1000 °C; (**c**) 0.1 s^{-1}-1100 °C; (**d**) 0.1 s^{-1}-1050 °C; (**e**) 1.0 s^{-1}-1050 °C; (**f**) 8.0 s^{-1}-1050 °C.

Figure 4d,f shows the prior austenite grains of SAE8620RH gear steel deformed at 1050 °C with different strain rates. Notably, no elongated, deformed austenite grains were observed, suggesting the occurrence of dynamic recrystallization of deformed austenite at 1050 °C within the strain rate range of 0.1–8.0 s^{-1}. At a strain rate of 0.1 s^{-1}, the average grain size of austenite was approximately 35.1 μm, although some grains exhibited significant growth, reaching a size of 43.5 μm. Upon further increasing the strain rate to 1.0 s^{-1}, the equiaxed austenite grains displayed a relatively uniform size distribution, resulting in an average grain size reduction of 31.2 μm. At a strain rate of 8.0 s^{-1}, the austenite grain size became more uniform, with an average size of 23.3 μm. In summary, the average grain size of deformed austenite exhibited a decrease as the strain rate increased. This phenomenon can be explained by the fact that the higher strain rate resulted in a

greater number of dislocations per unit volume, thereby providing more nucleation points for dynamic recrystallization. Additionally, the increased strain rate also reduced the time available for grain growth.

3.2. Establishment of the Strain Compensation Constitutive Model

Analysis of the true stress-strain curves revealed that the true stress was primarily influenced by three factors: deformation temperature, strain rate, and strain, during the thermal deformation of SAE8620RH gear steel. The purpose of the constitutive model was to investigate the relationship between them, which could be expressed as Equation (1) under high-temperature plastic deformation [35]:

$$\dot{\varepsilon} = \begin{cases} A_1\sigma^{n_1}\exp\left(-\frac{Q}{RT}\right)(\alpha\sigma < 0.8) \\ A_2\exp(\beta\sigma)\left(-\frac{Q}{RT}\right)(\alpha\sigma > 1.2) \\ A[\sinh(\alpha\sigma)]^n\exp\left(-\frac{Q}{RT}\right)(for\ all) \end{cases} \quad (1)$$

where, A_1, A_2, A, n, n_1 (N), β (mm^2), and α (mm^2. N^{-1}) are material-related parameters independent of deformation temperature. $\alpha = \beta/n_1$. A_1, A_2, A are the structural factors; n, n_1 are the stress indices. $\dot{\varepsilon}$ is the strain rate (s^{-1}), Q is the thermal deformation activation energy for hot deformation ($kJ{\cdot}mol^{-1}$). R is the molar gas constant (8.31 $J{\cdot}(mol{\cdot}K)^{-1}$, T is the thermodynamic temperature (K), and σ is the stress (MPa). Additionally, the comprehensive influence of temperature and strain rate on the thermal deformation behavior of metal can be formulated in terms of the Zener–Hollomon parameter (Z-parameter) through the following exponent-type Equation (2) [35]:

$$Z = \dot{\varepsilon}\exp\left(\frac{Q}{RT}\right) \quad (2)$$

The value of the material constants can be obtained separately by associating Equations (1) and (2) and performing logarithmic derivation. Detailed calculations are not shown in this paper due to numerous literature reports [9,20].

In Equations (1) and (2), only the effects of strain rate, deformation temperature, and stress on the flow behavior were considered. However, the effect of strain was ignored. In fact, the material-related parameters and thermal deformation activation energy have a strong correlation with strain [18]. To enhance the applicability of the constitutive model for the SAE8620RH gear steel and provide a more precise depiction of the stress-strain relationship, the influence of strain was incorporated into the model. The relationship between strain and stress can be inferred indirectly through an investigation of the variations in strain and material-related parameters. To ensure the accuracy of the derived constitutive equation, stress values were recorded at various deformation parameters using a strain interval of 0.05. By employing Equations (1) and (2) mentioned earlier, the material-related parameters were determined under different strain states (0.025–8.0 s^{-1}) and deformation temperatures (850–1100 °C) within the range of real strain (0.05–0.8).

The calculated material-related parameters of α, n, Q, and $\ln A$ in SAE8620RH gear steel at different strains are shown in Table 2. It was evident that these parameters were not constant but exhibited variations with strain. It can be seen that the calculated material-related parameters at different strains proved to be crucial for the precise formulation of the constitutive models. For instance, the hot deformation activation energy reached a peak value of 357 $kJ{\cdot}mol^{-1}$ at a strain of 0.3 and subsequently decreased gradually with increasing strain, down to 331 $kJ{\cdot}mol^{-1}$ at a strain of 0.8. It is generally believed that the number of movable slip systems is small at the beginning of deformation. However, as dislocations rapidly generate, they hinder crystal slip, resulting in an elevation of the hot deformation activation energy. As the strain increases, more slip systems begin to engage in sliding. Furthermore, deformation storage serves as a driving force for dynamic recovery,

thereby reducing the strain energy and causing a decrease in the activation energy for hot deformation activation energy.

Table 2. Material-related parameters calculated at different strains.

ε	α	n (N)	Q (kJ·mol^{-1})	ln$A$
0.05	0.01133	6.53	294.96	26.59
0.1	0.00967	6.71	322.07	29.11
0.15	0.00876	6.65	327.54	29.69
0.2	0.00833	6.48	342.23	31.13
0.25	0.00806	6.27	353.75	32.29
0.3	0.00787	6.03	357.25	32.69
0.35	0.00777	5.81	356.60	32.65
0.4	0.00772	5.61	354.44	32.45
0.45	0.00773	5.44	351.90	32.20
0.5	0.00775	5.30	349.88	31.98
0.55	0.00781	5.19	347.40	31.72
0.6	0.00784	5.08	344.22	31.38
0.65	0.00788	5.00	341.38	31.07
0.7	0.00791	4.95	339.06	30.80
0.75	0.00794	4.88	334.95	30.37
0.8	0.00799	4.82	331.28	29.97

The strain was found to have a close relationship with material-related parameters in the SAE8620RH gear steel, as indicated in Table 2. Therefore, it was imperative to determine the appropriate material constants, namely α, n, Q, and ln$A$. Through extensive comparative studies, it was observed that the 8th-degree polynomial expressed in Equation (3) provided the most accurate calculation results for capturing the variation relationship between the material-related parameters and strain.

$$\begin{cases} \alpha = B_0 + B_1\varepsilon + B_2\varepsilon^2 + B_3\varepsilon^3 + B_4\varepsilon^4 + B_5\varepsilon^5 + B_6\varepsilon^6 + B_7\varepsilon^7 + B_8\varepsilon^8 \\ n = C_0 + C_1\varepsilon + C_2\varepsilon^2 + C_3\varepsilon^3 + C_4\varepsilon^4 + BC_5\varepsilon^5 + C_6\varepsilon^6 + C_7\varepsilon^7 + C_8\varepsilon^8 \\ Q = D_0 + D_1\varepsilon + D_2\varepsilon^2 + D_3\varepsilon^3 + D_4\varepsilon^4 + D_5\varepsilon^5 + D_6\varepsilon^6 + D_7\varepsilon^7 + D_8\varepsilon^8 \\ lnA = E_0 + E_1\varepsilon + E_2\varepsilon^2 + E\varepsilon^3 + E_4\varepsilon^4 + E_5\varepsilon^5 + E_6\varepsilon^6 + E_7\varepsilon^7 + E_8\varepsilon^8 \end{cases} \quad (3)$$

The polynomial coefficients fitted using Equation (3) and the data in Table 2 are presented in Table 3. The resulting calculated values and the corresponding fitted curves are depicted in Figure 5. Their linear correlations were all found to be above 0.999, indicating a high level of reliability for the fitted 8th-degree polynomial.

Table 3. Fitting coefficients of the 8th-order polynomial.

α		n		Q (kJ·mol^{-1})		ln$A$	
B0	0.01451	C0	5.88686	D0	86.60001	E0	7.22426
B1	−0.08544	C1	19.72714	D1	8464.95696	E1	787.75528
B2	0.5128	C2	−167.35935	D2	−125,626.83041	E2	−11,712.98729
B3	−1.77118	C3	674.78087	D3	991,339.23108	E3	92,571.73376
B4	3.51408	C4	−1806.99553	D4	−4530770	E4	−423,127.06613
B5	−3.62587	C5	3276.56793	D5	12,638,900	E5	1,179,530
B6	1.19417	C6	−3765.56793	D6	22,949,700	E6	−2039660
B7	0.82028	C7	2437.43677	D7	13,366,400	E7	2,137,290
B8	−0.57123	C8	−672.61027	D8	33,171,100	E8	1,243,440

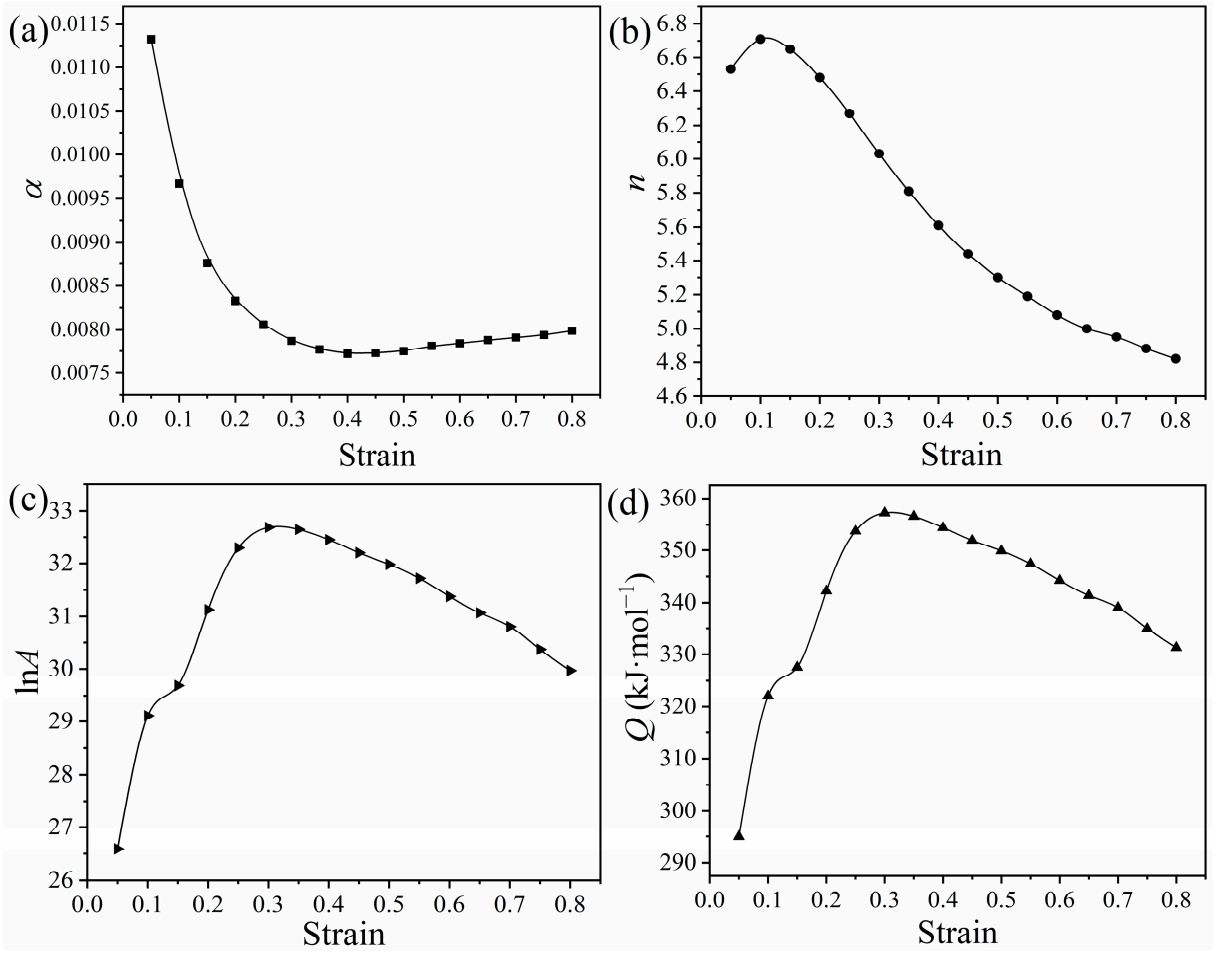


Figure 5. Relationship between material-related parameters under the 8th order polynomial fitting in SAE8620RH gear steel (**a**) α; (**b**) n; (**c**) Q; (**d**) ln$A$.

By substituting the functions of material-related parameters, fitted deformation activation energy, and Equation (2) into Equation (1), a novel strain-compensated constitutive equation for stress and thermal deformation parameters was developed in Equation (4):

$$\sigma = \frac{1}{\alpha(\varepsilon)} \ln \left\{ \left(\frac{Z(\varepsilon)}{A(\varepsilon)} \right)^{\frac{1}{n(\varepsilon)}} + \left[\left(\frac{Z(\varepsilon)}{A(\varepsilon)} \right)^{\frac{2}{n(\varepsilon)}} + 1 \right]^{\frac{1}{2}} \right\} \quad (4)$$

In order to assess the accuracy of the strain-compensated constitutive model (6) established for the SAE8620RH gear steel in predicting flow stress, the stress values calculated using Equation (4) were compared against experimental data, as shown in Figure 6. The new strain-compensated constitutive model yielded predicted values that were generally in agreement with experimental data at deformation temperatures ranging from 850 to 1100 °C and strain rates between 0.02 and 8.0 s^{-1}. However, it was important to acknowledge that the predicted values at lower deformation temperatures, specifically at a strain rate of 8.0 s^{-1}, exceeded the corresponding experimental data. This discrepancy can be attributed to the significant heat generated during instantaneous deformation at a high strain rate, which elevated the effective deformation temperature and consequently led to reduced actual stress levels.

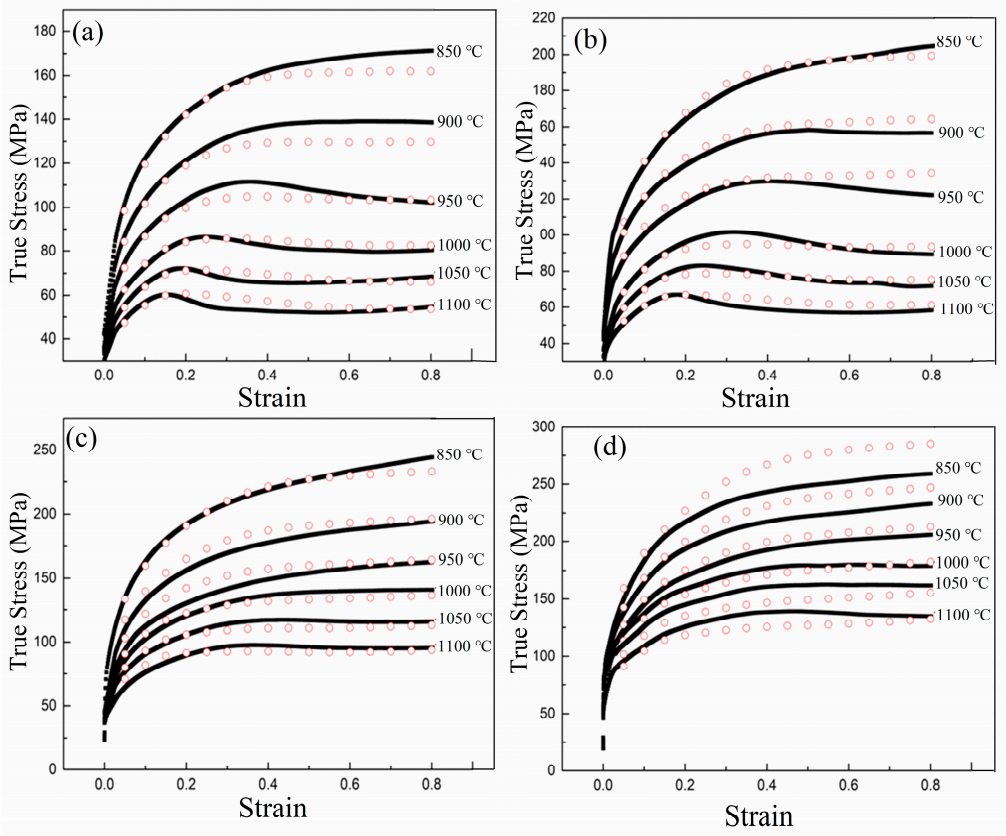


Figure 6. The calculated tress compared against the experimental data under different strain rates (**a**) 0.02 s^{-1}; (**b**) 0.05 s^{-1}; (**c**) 0.1 s^{-1}; (**d**) 1.0 s^{-1}.

To conduct a comprehensive evaluation of the prediction accuracy of the strain compensation constitutive model, the R value and the AARE value were used to analyze and compare the consistency between the predicted results and experimental data. The expressions for correlation coefficient and AARE are as in Equations (5) and (6):

$$AARE(\%) = \frac{1}{N}\sum_{i=1}^{N}\left|\frac{E_i - P_i}{E_i}\right| \quad (5)$$

$$R = \frac{\sum_{i=1}^{N}(E_i - \bar{E})(P_i - \bar{P})}{\sqrt{\sum_{i=1}^{N}(E_i - \bar{E})^2 \sum_{i=1}^{N}(P_i - \bar{P})^2}} \quad (6)$$

where, E_i is the measured value; P_i is the predicted value; N is the number of selected true stress data.

It is important to note that the accuracy of the R value is contingent upon the quantity of experimental data available. The value of AARE effectively characterizes the average absolute value of the relative error between the experimental data and the predicted values, thus providing a more precise assessment of the prediction accuracy of the strain compensation constitutive equation. It is widely accepted that an AARE value within a 5% margin is indicative of high prediction accuracy. The comparison between predicted values and experimental data is illustrated in Figure 7. The R value and AARE value were 0.978 and 4%, respectively, both falling within the permissible error range. This suggested that the predicted values derived from the new strain compensation constitutive equation for SAE8620RH gear steel could be considered reliable within the range of deformation temperatures (850–1100 °C) and strain rates (0.02–8.0 s^{-1}).

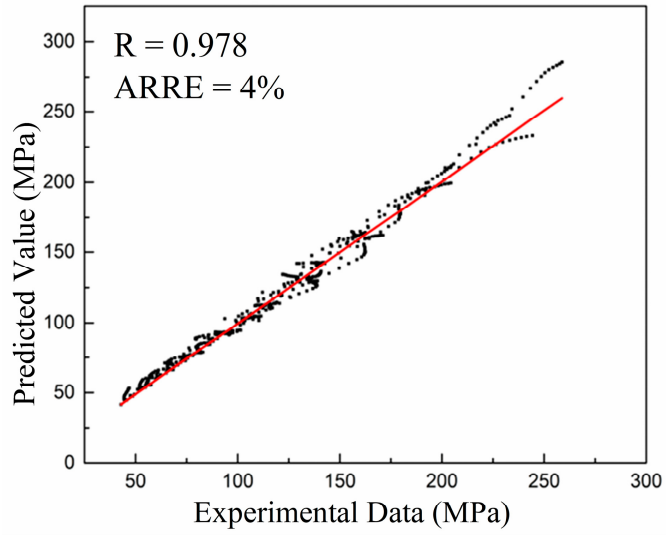


Figure 7. The comparison between predicted values and experimental data.

3.3. Research and Construction of a Processing Map

Based on the constitutive laws of materials, the total energy (p) input during deformation at high temperatures is mainly used for microstructural transformation consumption and plastic deformation consumption. The corresponding expression is [24]:

$$P = \sigma\dot{\varepsilon} = G + J = \int_0^{\dot{\varepsilon}} \sigma d\dot{\varepsilon} + \int_0^{\sigma} \dot{\varepsilon} d\sigma \tag{7}$$

where, σ is the flow stress (MPa), $\dot{\varepsilon}$ is the strain rate, and G is the energy consumed by the plastic transformation (G content). J is the energy consumed by the microstructural transformation (J co-content).

When the strain and deformation temperatures are held constant, the ratio of J and G is determined by the strain rate sensitivity index, m, (Equation (8)) [36]. Typically, the value of m falls within the range of 0–1. A value of 1 signifies that the plastic deformation of the metal material is in an optimal state, resulting in the maximum value of J_{max}.

$$m = \frac{dJ}{dG} = \frac{\dot{\varepsilon} d\sigma}{\sigma d\dot{\varepsilon}} = \left(\frac{\partial ln\sigma}{\partial \dot{\varepsilon}}\right)_{T,\varepsilon} \tag{8}$$

$$J_{max} = \frac{\sigma\dot{\varepsilon}}{2} \tag{9}$$

The power dissipation efficiency, denoted as η, is defined as the ratio of the energy consumed for the evolution of the microstructure during thermal deformation to $J_{\max}$ (Equation (10)).

$$\eta = \frac{J}{J_{max}} \tag{10}$$

In the context of metals undergoing thermoplastic deformation, it is observed that a higher value of η corresponds to a more favorable thermoplastic deformation effect. However, it is important to note that the suitability of thermal process parameters for thermal processing cannot solely rely on a large value of η, as the presence of microstructure defects must also be considered. In certain cases, defective microstructures may coexist with a high η value. Consequently, it becomes necessary to construct an instability map using the instability criterion in conjunction with the power dissipation map in order to thoroughly investigate the thermal working process of the SAE8620RH gear steel.

Many scholars have put forth various instability criteria derived from the DMM model theory. Notably, Prasad's instability criteria and Murty's instability criteria have garnered

significant recognition for their accurate results. Upon analyzing and calculating both of the two instability criteria, it is evident that Murty's criterion is better suited for analyzing the thermal working process of SAE8620RH gear steel. Consequently, the subsequent section will focus on the analysis using Murty's instability criterion.

When the deformation temperature and strain are determined, the flow stress and strain rate satisfy Equation (11) [37]:

$$\sigma = \mathrm{K}\dot{\varepsilon}^{m} \tag{11}$$

where K is generally considered to be a constant. Combined with the above equation, an expression for J can be obtained:

$$J = \int_0^{\sigma} \dot{\varepsilon} d\sigma = \frac{m}{m+1}\sigma\dot{\varepsilon} \tag{12}$$

Therefore, η can be defined as Equation (13) [38]:

$$\eta = \frac{2m}{m+1} \tag{13}$$

Murty and Rao et al. have highlighted that the value of m in alloy steel cannot be considered constant due to the impact of alloying elements [39]. To accurately develop the processing map for SAE8620RH gear steel, Equation (13) can be modified as Equation (14):

$$\eta = \frac{J}{J_{-max}} = \frac{P-G}{P/2} = 2\left(1-\frac{G}{P}\right) = 2\left(1-\frac{1}{\sigma\dot{\varepsilon}}\int_0^{\dot{\varepsilon}} \sigma d\dot{\varepsilon}\right) \tag{14}$$

Based on the above theory and equations, Murty proposed a destabilization criterion suitable for any alloy steel [29]:

$$\xi\left(\dot{\varepsilon}\right) = 2m - \eta < 0 \tag{15}$$

where, $\xi\left(\dot{\varepsilon}\right)$ represents the instability parameter, which enables the determination of whether the metal is destabilized or not based on the given thermal deformation parameters. It is evident that when the thermal deformation parameters meet the conditions stated in Equation (15), flow instability occurs during the hot working deformation process.

To enhance the accuracy of data representation in the construction of processing maps, the application of the third-degree polynomial method is employed to nonlinearly fit the $\ln\sigma - \ln\dot{\varepsilon}$ relationship of metal material, as depicted in the subsequent Equation (16) [40]:

$$\ln\sigma = \mathrm{a} + \mathrm{b}\ln\dot{\varepsilon} + c\left(\ln\dot{\varepsilon}\right)^2 + d\left(\ln\dot{\varepsilon}\right)^3 \tag{16}$$

Taking the derivative of Equation (17) yields:

$$\frac{\partial\ln\sigma}{\partial\ln\dot{\varepsilon}} = b + 2c\ln\dot{\varepsilon} + 3d\left(\ln\dot{\varepsilon}\right)^2 = m \tag{17}$$

The functional relationship curve of $\ln\sigma - \ln\dot{\varepsilon}$ for SAE8620RH gear steel is shown in Figure 8. It is evident that $\ln\sigma - \ln\dot{\varepsilon}$ did not conform to a linear relationship, but rather exhibited nonlinearity. This observation further signified that the strain rate sensitivity index was variable and could not be treated as a constant. Then the value of m at different strains could be obtained by fitting the curves in Figure 8.

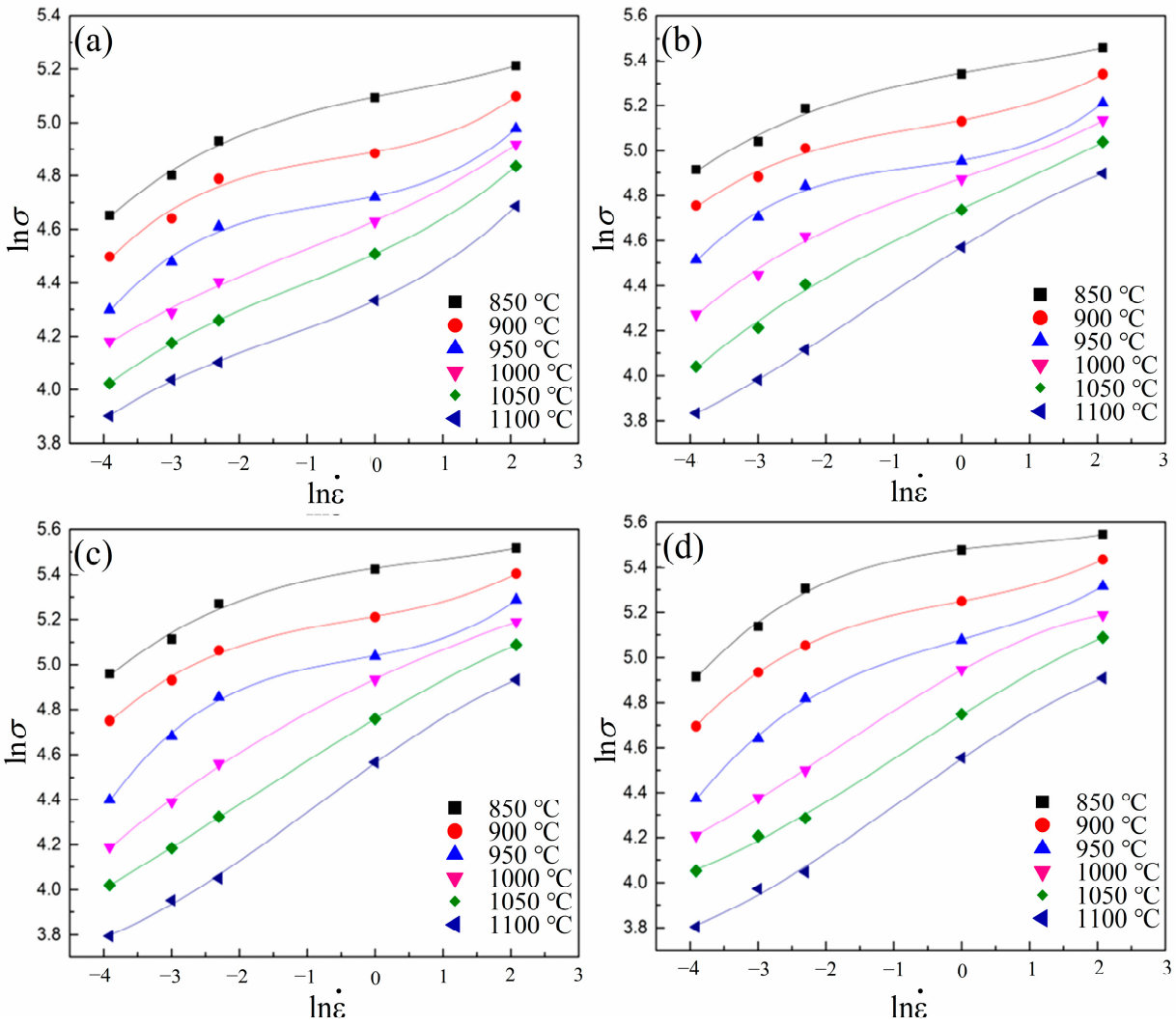


Figure 8. Plot of lnσ as a function of ln$\dot{\varepsilon}$ at different strain: (**a**) 0.1; (**b**) 0.3; (**c**) 0.5; (**d**) 0.7.

By utilizing Equation (14) and integrating the stress-strain data of the SAE8620RH gear steel across various deformation conditions, the numerical fitting enables the calculation of the value of η. Consequently, the power dissipation maps (2D contour maps) of SAE8620RH gear steel at different strains were plotted, as shown in Figure 9. It is important to note that, for the purpose of data visualization, the values of η presented in Figure 9 have been multiplied by 100. The power dissipation efficiency in the SAE8620RH gear steel exhibited a discernible upward trend as the strain increased, while maintaining a constant deformation temperature and strain rate. While the deformation temperature ranged between 1050 and 1100 °C with a strain rate of 0.02 s^{-1}, the value of η exhibited a decrease with increasing strain. The phenomenon is similar to that reported by Han et al. in their study on stainless steel. Han et al. attributed this phenomenon to the low energy consumption resulting from grain boundary migration, which in turn affected dynamic recrystallization at high temperatures and low strain rates [41]. Furthermore, the deformation temperature was found to impact the power dissipation efficiency, with an increase in η observed as the deformation temperature rose, particularly at medium to high strain rates ($\varepsilon \geq 0.3\ s^{-1}$).

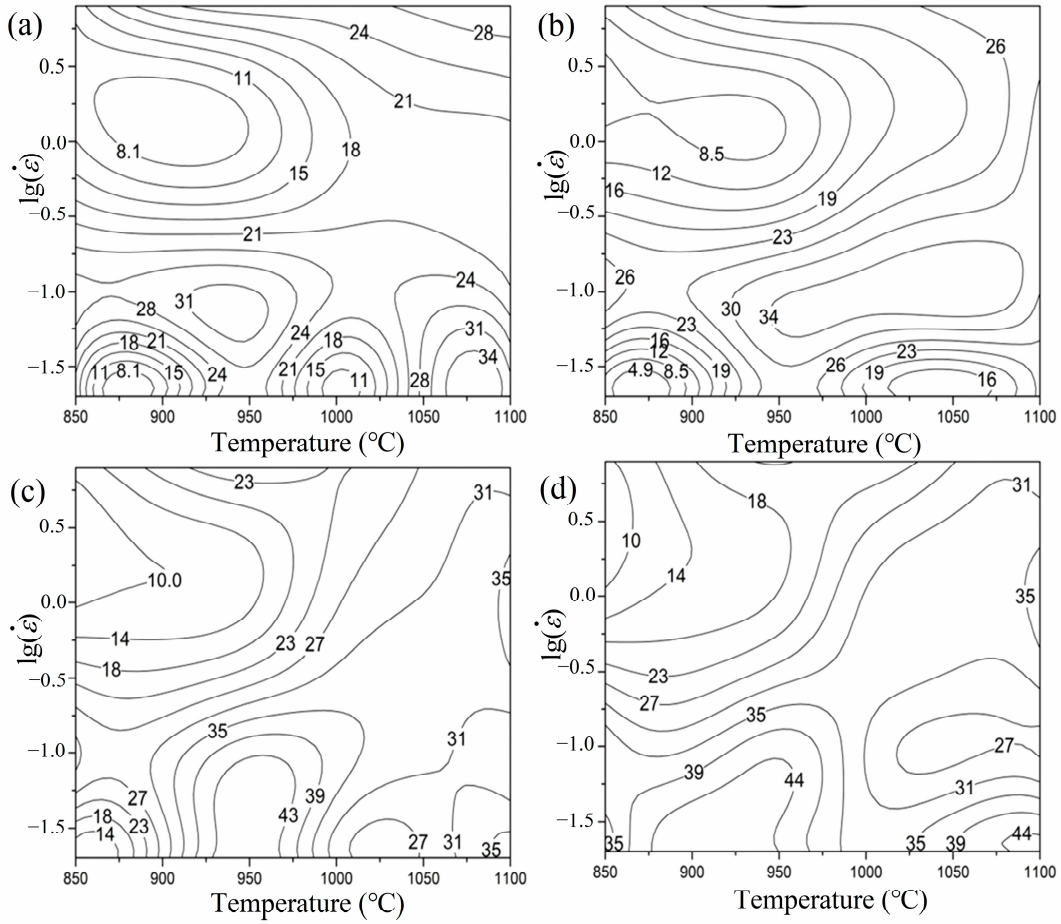


Figure 9. Power dissipation maps (2D contour maps) for SAE8620RH gear steel at different strains (**a**) 0.1; (**b**) 0.3; (**c**) 0.5; (**d**) 0.7.

Combined with the evolution of austenite grains in Figure 4 and the variation of power dissipation efficiency at different deformation parameters in Figure 9, it can be found that the power dissipation efficiency was closely related to the microstructure. Previous research has indicated that a value of η greater than 0.3 typically signifies the occurrence of dynamic recrystallization, while a value between 0.2 and 0.3 suggests dynamic recovery. Consequently, it is advisable to prioritize the deformation parameters with higher values. When the deformation parameters are at a high value of η conditions and fall outside the flow instability domain, it is plausible to consider that a more favorable microstructure can be achieved in the SAE8620RH gear steel. Conversely, when the values of η are low, it is not advisable to engage in thermal deformation at this specific parameter, regardless of whether the SAE8620RH gear steel experiences flow instability or not.

As shown in Figure 9a, there were two peak efficiency domains at a strain of 0.1 s^{-1}. Both peak values of η surpassed 0.3, suggesting that favorable microstructure can be achieved when SAE8620RH gear steel deforms under the peak efficiency conditions. In the vicinity of the peak η domain, the alteration in η value in response to variations in thermal deformation parameters was minimal, indicating a nearly unchanged deformation mechanism in SAE8620RH gear steel. Consequently, it can be considered as a preferred choice for the practical production of SAE8620RH gear steel, provided no flow instabilities occur. At a strain of 0.3 (Figure 9b), the domain of peak η value decreased by one, indicating a reduction in the appropriate hot working region for SAE8620RH gear steel. With further increases in strain (Figure 9c), the domain with η values greater than 0.3 expanded. At a strain of 0.7 (Figure 9d), the values of η were predominantly greater than 0.3 for strain rates below 0.1 s^{-1} and within a deformation temperature range of 850 to 1100 °C. However,

when the deformation temperature was below 900 °C and the strain rate exceeded 0.3 s^{-1}, the calculated values of η were lower than 0.3. It suggested that the SAE8620RH gear steel primarily underwent dynamic recovery. Based on the analysis of power dissipation efficiency, it can be inferred that the optimal thermal processing parameters for the SAE8620RH gear steel, with a strain of 0.7, are a strain rate ranging from 0.02 to 1.0 s^{-1} for deformation at temperatures between 1000 and 1100 °C and a strain rate ranging from 0.02 to 0.1 s^{-1} for deformation at temperatures between 850 and 900 °C.

The magnitude of the η value is a criterion, albeit not the sole factor, for evaluating the hot workability of metals. In instances where thermal processing parameters obtain high η values, it is imperative to examine the associated microstructure and ascertain the presence of flow instability. This analysis aids in identifying the optimal deformation parameters. By utilizing Equation (15) and incorporating the previously calculated values of m and η, the instability parameter was determined. Subsequently, the instability maps of the SAE8620RH gear steel were graphed. Afterwards, the instability maps were overlaid onto the power dissipation maps, resulting in the acquisition of processing maps for the SAE8620RH gear steel at temperatures ranging from 850 to 1100 °C and strain rates ranging from 0.02 to 8.0 s^{-1}, as depicted in Figure 10. The shaded area within the maps denotes the region of flow instability.

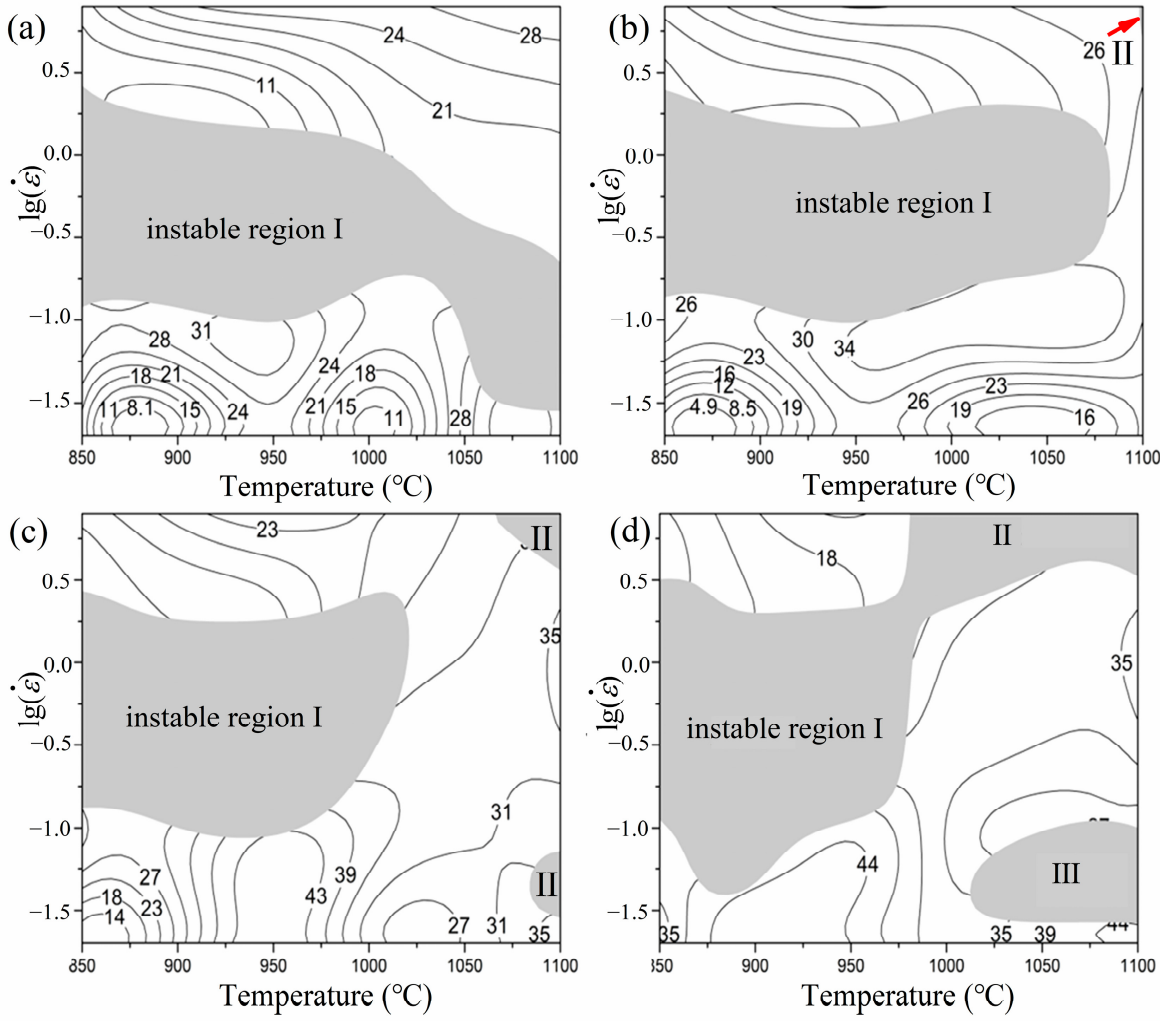


Figure 10. The thermal processing maps of SAE8620RH gear steel based on Murty's instability criterion under different strains (**a**) 0.1; (**b**) 0.3; (**c**) 0.5; (**d**) 0.7.

An observable alteration in the flow instability region within the processing map occurred with an increase in strain. At a strain 0.1, flow instability occurred in the respective

ranges of the strain rates and the temperatures of 0.1–3 s^{-1} and 850–1000 °C, as well as 0.1–0.05 s^{-1} and 1050–1100 °C. Notably, the flow instability region at a deformation temperature of 1050–1100 °C and a strain rate of 0.1–0.05 s^{-1} was found to be in a peak efficiency domain. This finding supported the previous assertion that higher values of η resulted in increased energy consumption for microstructure evolution. Dynamic recrystallization may occur, while flow instability may also form due to microstructure defects such as uneven deformation during thermal deformation.

At a strain of 0.3, the flow instability domain was expanded within the strain rate range of 0.1 to 3.0 s^{-1}. Furthermore, the flow instability domain also occurred at high temperatures with high strain rates, as depicted by the limited area indicated by the red arrow in the upper right corner of Figure 10b. When the strain reached 0.5, flow instability region I decreased, while flow instability region II in the upper right corner expanded comparatively, and a new flow instability region III (SAE8620RH gear steel deformed at high temperatures with low strain rates) emerged. The findings suggested there might be a critical strain for flow-instable microstructure formed during the strain range of 0.3–0.5 in SAE8620RH gear steel. Additionally, both flow instability regions II and III were observed at a high temperature of 1100 °C. Therefore, careful attention should be given to controlling the strain rate during the rough rolling process at high temperatures. Based on the power dissipation efficiency and the instability map, it is recommended to conduct hot deformation processing at 950 °C with low strain rates of approximately 0.1–0.025 s^{-1} for a set strain of 0.5 in SAE8620RH gear steel.

By further increasing the strain to 0.7, the amplification of the flow instability region was to be significant. This observation serves as evidence for an increased propensity for instability resulting from deformation at high temperatures. The processing map analysis revealed the existence of two optimal ranges of thermal processing parameters for SAE8620RH gear steel: deformation at 900–950 °C with strain rates of 0.02–0.05 s^{-1}, and deformation at 1000–1100 °C with an astrain rate of 0.3–1.0 s^{-1}. It is important to note that low strain rates are not suitable for industrial production. In order to enhance efficiency, the more optimized process parameter range is deformation at 1000–1100 °C with strain rates ranging from 0.3–1.0 s^{-1}.

In the processing map, peak values of η indicate distinctive microstructural evolution. However, the presence of defects such as wedge cracks often results in high η values as well. To further substantiate the reliability of the processing maps obtained for SAE8620RH gear steel, an analysis of the microstructure is necessary.

Figure 11 displays the boundaries of prior austenite grains at a strain of 0.7 under the corresponding parameters of different regions of the SAE8620RH gear steel. Deformed at 900 °C with 0.1 s^{-1} (Figure 11a), the η value approached 0.3, accompanied by an increased presence of dynamically recrystallized grains. The congruence between the microstructure and the η value was notable. However, the presence of large, deformed grains suggested the possibility of localized inhomogeneous deformation. Incomplete dynamic recrystallization and uneven grain size distribution rendered the SAE8620RH gear steel unsuitable for hot working under the conditions. Upon increasing the strain rate to 1.0 s^{-1} (Figure 11b), the calculated η value decreased to approximately 0.14, indicating minimal consumption of deformation storage energy for microstructure evolution. Correspondingly, the quantity of dynamic recrystallization grains exhibited a decrease and was substituted by a substantial number of deformed elongated grains and deformation bands. Consequently, this thermal process parameter was deemed unsuitable. Deformed at 950 °C with 0.05 s^{-1} (Figure 11c), the prior austenite grains were characterized by a dense and uniform distribution. However, as the temperature escalated to 1100 °C with a strain rate of 0.05 s^{-1} (Figure 11d), the average grain size experienced a significant increase with an uneven distribution of grains. Additionally, the presence of abnormally coarse grains resulted in suboptimal mechanical properties. Hence, it became imperative to prevent the occurrence of heterogeneous microstructures.

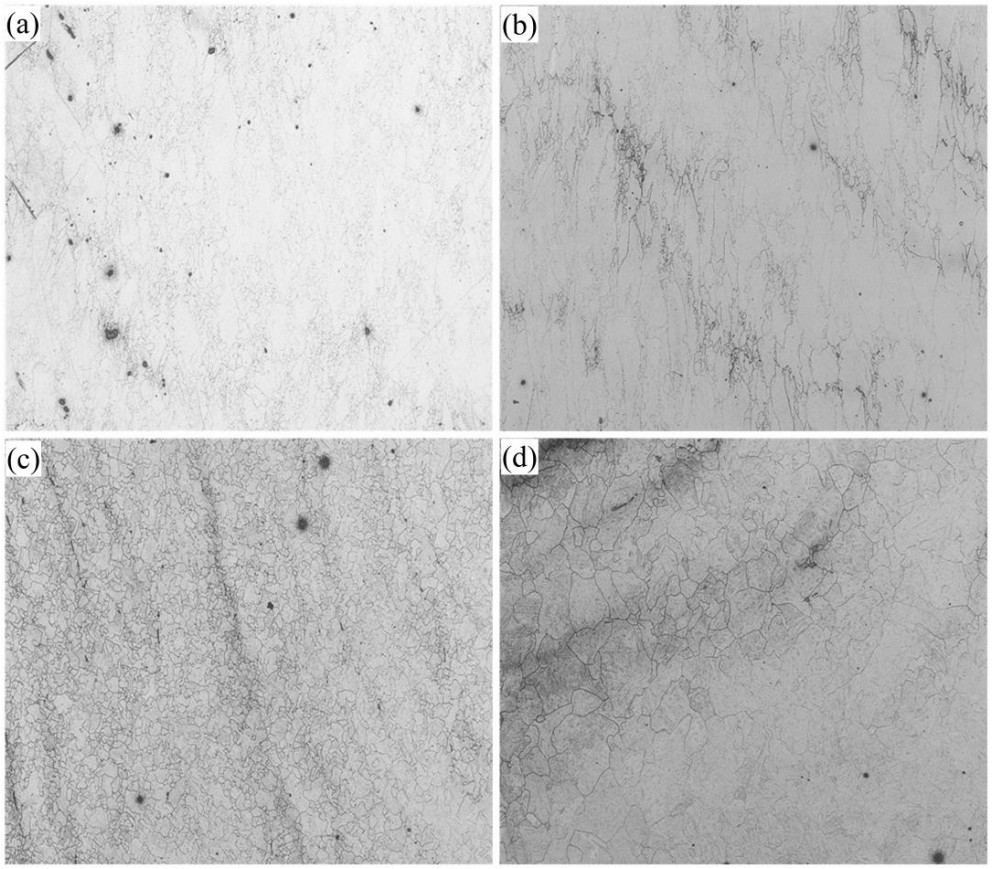


Figure 11. The microstructure of gear steel under different deformation conditions with strain of 0.7: (**a**) 900 °C-0.1 s^{-1}; (**b**) 900 °C-1.0 s^{-1}; (**c**) 950 °C-0.05 s^{-1}; (**d**) 1100 °C-0.05 s^{-1}.

In relation to the power dissipation map, the value of η exhibited a decline from 0.44 at 950 °C to 0.32 at 1100 °C. The trend in power dissipation efficiency aligned with the results of the microstructure evolution. Furthermore, the specimen subjected to a strain of 0.7 at 1050 °C with a rate of 1.0 s^{-1} demonstrated the attainment of relatively fine and homogeneous equiaxed austenite grains, as depicted in Figure 4e. The corresponding value of η was approximately 0.35. This combination of thermal processing parameters proved to be optimal in terms of both microstructure and power dissipation efficiency.

It was evident from the unsuitable thermal process parameters identified that they were situated within the instability regionIbased on the microstructure and power dissipation map. Conversely, the parameters conducive to thermal processing were found within the stability region. Consequently, it can be posited that the thermal processing map derived using Murty's criterion was reasonably precise, thereby offering valuable guidance in the optimization of process parameters for SAE8620RH gear steel.

4. Conclusions

The hot deformation behavior of the SAE8620RH gear steels was investigated by a single-pass hot compression test in this paper. Furthermore, a newly developed strain compensation constitutive model and processing maps in accordance with Murty's criterion were developed using the acquired experimental data. Finally, the optimum hot working process for SAE8620RH gear steel was obtained. The main conclusions are as follows:

(1) The material-related parameters were variable with strain, and their relationship was mathematically expressed as a highly reliable 8th-order polynomial. The new strain compensation constitutive model, considering the coupling effects of strain, strain rate, and deformation temperature, was established. The obtained R value of 0.978 and the ARRE value of approximately 4% demonstrate high accuracy.

(2) The power dissipation efficiency determined by Murty's criterion exhibited a positive correlation with strain. The thermal process parameters with high values of η may be within the flow instability domain due to microstructure defects, such as uneven deformation.
(3) As strain increased, the flow instability domain considerably expanded towards the high deformation temperature region. Notably, at a strain of 0.7, it became imperative to avoid three distinct flow instability domains. Among these, one was situated within the low deformation temperature range, accompanied by medium strain rates, while the remaining two were located within deformation temperatures surpassing 1000 °C.
(4) Microstructure analysis further demonstrated the accuracy of the thermal processing map constructed by Murty's criterion. The optimum hot working parameters for SAE8620RH gear steel at a strain of 0.7 were within the temperature range of 1000–1100 °C and the strain rate range of 0.3–1.0 s^{-1}, due to high η values exceeding 0.3 and equiaxial dynamic recrystallization microstructure.

Author Contributions: Conceptualization, L.L. and R.Z.; methodology, S.C.; software, S.C.; validation, L.L.; formal analysis, S.C. and L.L.; investigation, S.C. and L.L.; resources, L.L. and R.Z.; data curation, S.C. and L.L.; writing—original draft preparation, S.C.; writing—review and editing, S.C., L.L. and R.Z.; visualization, L.L.; supervision, L.L.; project administration, L.L. and R.Z.; funding acquisition, R.Z. All authors have read and agreed to the published version of the manuscript.

Funding: This research was funded by the 2022 Shaoguan Science and Technology Planning Project, grant number 220606114532986, and the Guangzhou Municipal Science and Technology Project, grant number 202007020007.

Data Availability Statement: The data presented in this study are available upon request from the corresponding author.

Conflicts of Interest: The authors declare no conflict of interest.

References

1. Llu, X.; Zhan, D.P.; Jiang, Z.H.; Zhang, H.S.; An, J.; Li, T.; Sun, D.L.; Wu, Y. Analysis on inclusions of SAE8620RH gear steel produced by EAF→lF→VD→CC. *Steel Mak.* **2022**, *38*, 58–65.
2. Cao, Y.G.; Xu, L.; Shi, J.; Wang, X.K.; Wang, M.Q. Effect of hardenability of SAE8620H on i-tsdistortion by heat treatment. *J. Iron Steel Res.* **2016**, *28*, 47–51.
3. Zhang, H.Q.; Xie, Y.; Cheng, G.G.; Chen, L.; Kou, Y.S. Characteristics of inclusions in high sulfur gear steel SAE8620H hot-rolled round bar. *Iron Steel* **2013**, *48*, 70–75.
4. Ma, F.G. Isothermal normalization process for SAE8620RH steel. *Met. Heat Ttreatment* **2010**, *35*, 120–123.
5. Li, X.D. Research on Carburizing Process for Material SAE8620RH. *Automot. Technol.* **2008**, *10*, 59–62.
6. Wang, Z.; Wang, X.N.; Zhu, Z.S. Characterization of high-temperature deformation behavior and processing map of tb17 titanium alloy. *J. Alloys Compd.* **2017**, *692*, 149–154. [CrossRef]
7. Song, T.; Xu, S.Y.; Li, Y.L.; Ding, H. Hot deformation and dynamic recrystallization behavior of a cu-9ni-6sn-0.04cr alloy. *Mater. Today Commun.* **2023**, *35*, 105828. [CrossRef]
8. Derazkola, H.A.; Eduardo García, G.; Murillo-Marrodán, A.; Méresse, D. Review on dynamic recrystallization of martensitic stainless steels during hot deformation: Part I—Experimental study. *Metals* **2021**, *11*, 572. [CrossRef]
9. Song, Y.H.; Cai, Z.H.; Zhao, G.H.; Li, Y.G.; Li, H.Y.; Zhang, M.G. Hot deformation behavior of 309L stainless stee. *Mater. Today Commun.* **2023**, *36*, 106877. [CrossRef]
10. Zhang, K.; Zhang, T.H.; Zhang, M.Y.; Chen, Z.H.; Pan, H.B.; Yang, G.W.; Cao, Y.G.; Li, Z.D.; Zhang, X. Hot deformation behavior, dynamic recrystallization mechanism and processing maps of Ti–V microalloyed high strength steel. *J. Mater. Res. Technol.* **2023**, *25*, 4201–4215. [CrossRef]
11. Shi, Z.X.; Yan, X.F.; Duan, C.H. Characterization of hot deformation behavior of gh925 superalloy using constitutive equation, processing map and microstructure observation. *J. Alloys Compd.* **2015**, *652*, 30–38. [CrossRef]
12. Zhang, Y.L.; Qu, S.G.; Lai, F.Q.; Qin, H.D.; Huang, L.M.; Li, X.Q. Effect of quenching temperature on microstructure and rolling contact fatigue behavior of 17Cr2Ni2MoVNb steel. *Metals* **2018**, *8*, 735. [CrossRef]
13. Liao, W.H.; Tsai, C.W.; Tzeng, Y.C.; Wang, W.R.; Chen, C.S.; Yeh, J.W. Exploring hot deformation behavior of equimolar cocrfeni high-entropy alloy through constitutive equations and microstructure characterization. *Mater. Charact.* **2023**, *205*, 1044–5083. [CrossRef]
14. Rajput, S.K.; Chaudhari, G.P.; Nath, S.K. Characterization of hot deformation behavior of a low carbon steel using processing maps, constitutive equations and zener-hollomon parameter. *J. Mater. Process. Technol.* **2016**, *237*, 113–125. [CrossRef]

15. Wei, W.; Wei, K.X.; Fan, G.J. A new constitutive equation for strain hardening and softening of fcc metals during severe plastic deformation. *Acta Mater.* **2008**, *56*, 4771–4779. [CrossRef]
16. Phaniraj, C.; Samantaray, D.; Mandal, S.; Bhaduri, A.K. A new relationship between the stress multipliers of garofalo equation for constitutive analysis of hot deformation in modified 9Cr–1Mo (P91) steel. *Mater. Sci. Eng. A* **2011**, *528*, 6066–6071. [CrossRef]
17. Xia, Y.Q.; Shu, X.D.; Zhang, Q.D.; Pater, Z.; Li, Z.X.; Xu, H.J.; Ma, Z.; Xu, C. Modified Arrhenius constitutive model and simulation verification of 2A12-T4 aluminum alloy during hot compression. *J. Mater. Res. Technol.* **2023**, *26*, 1325–1340. [CrossRef]
18. Cai, J.; Li, F.G.; Liu, T.Y.; Chen, B.; He, M. Constitutive equations for elevated temperature flow stress of Ti–6Al–4V alloy considering the effect of strain. *Mater. Des.* **2011**, *32*, 1144–1151. [CrossRef]
19. Wang, J.; Zhao, G.Q.; Chen, L.; Li, J.L. A comparative study of several constitutive models for powder metallurgy tungsten at elevated temperature. *Mater. Des.* **2016**, *90*, 91–100. [CrossRef]
20. Chen, G.; Yao, Y.C.; Jia, Y.Z.; Su, B.; Liu, G.Y.; Zeng, B. Hot deformation constitutive equation and plastic instability of 30Cr4MoNiV ultra-high-strength steel. *Metals* **2021**, *11*, 769. [CrossRef]
21. Lu, J.; Song, Y.L.; Hua, L.; Zheng, K.L.; Dai, D.G. Thermal deformation behavior and processing maps of 7075 aluminum alloy sheet based on isothermal uniaxial tensile tests. *J. Alloys Compd.* **2018**, *767*, 856–869. [CrossRef]
22. Tafone, A.; Pili, R.; Pihl Andersen, M.; Romagnoli, A. Dynamic modelling of a compressed heat energy storage (chest) system integrated with a cascaded phase change materials thermal energy storage. *Appl. Therm. Eng.* **2023**, *226*, 120256. [CrossRef]
23. Prasad, Y.V.R.K.; Gegel, H.L.; Doraivelu, S.M.; Malas, J.C.; Morgan, J.T.; Lark, K.A.; Barker, D.R. Modeling of dynamic material behavior in hot deformation: Forging of Ti-6242. *Metall. Trans. A* **1984**, *15*, 1883–1892. [CrossRef]
24. Prasad, Y.V.R.K. Processing maps: A status report. *J. Mater. Eng. Perform.* **2003**, *12*, 638–645. [CrossRef]
25. Mohanraj, P.; Sivakumar, R.; Joseph, A. Omnipresent instability criterion of birefringent kundu-eckhaus model with nonic nonlinearity. *Optik* **2022**, *265*, 169482. [CrossRef]
26. Lich, L.V.; Shimada, T.; Wang, J.; Kitamura, T. Instability criterion for ferroelectrics under mechanical/electric multi-fields: Ginzburg-landau theory based modeling. *Acta Mater.* **2016**, *112*, 1–10. [CrossRef]
27. Jin, K.; Guo, X.Z.; Tao, J.; Wang, H.; Kim, N.; Gu, Y. A model of one-surface cyclic plasticity with lemaitre damage criterion for plastic instability prediction in the incremental forming process. *Int. J. Mech. Sci.* **2016**, *114*, 88–97. [CrossRef]
28. Raj, R. Development of a processing map for use in warm-forming and hot-forming processes. *Metall. Trans. A* **1981**, *12*, 1089–1097. [CrossRef]
29. Murty, S.V.S.N.; Rao, B.N. On the development of instability criteria during hotworking with reference to in 718. *Mater. Sci. Eng. A* **1998**, *254*, 76–82. [CrossRef]
30. Shi, X.Z.; Du, S.W.; Chen, S.H. Analysis of processing performance of medium carbon steel based on processing map. *J. Iron Steel Res.* **2019**, *31*, 31–39.
31. Zhong, L.W.; Gao, W.L.; Feng, Z.H.; Lu, Z.; Zhu, C.C. Hot deformation characterization of as-homogenized Al-Cu-Li X2a66 alloy through processing maps and microstructural evolution. *J. Mater. Sci. Technol.* **2019**, *35*, 2409–2421. [CrossRef]
32. Savaedi, Z.; Motallebi, R.; Mirzadeh, H. A review of hot deformation behavior and constitutive models to predict flow stress of high-entropy alloys. *J. Alloys Compd.* **2022**, *903*, 163964. [CrossRef]
33. Chen, S.J.; Li, L.J.; Peng, Z.W.; Huo, X.D.; Gao, J.X. Strain-induced precipitation in Ti microalloyed steel by two-stage controlled rolling process. *J. Mater. Res. Technol.* **2020**, *9*, 15759–15770. [CrossRef]
34. Zheng, S.J.; Yuan, X.H.; Gong, X.; Le, T.; Ravindra, A.V. Hot deformation behavior and microstructural evolution of an Fe-Cr-W-Mo-VC steel. *Metall. Mater. Trans. A* **2019**, *50*, 2342–2355. [CrossRef]
35. Dehghan-Manshadi, A.; Barnett, M.R.; Hodgson, P.D. Recrystallization in AISI 304 austenitic stainless steel during and after hot deformation. *Mater. Sci. Eng. A* **2008**, *485*, 664–672. [CrossRef]
36. Shalbafi, M.; Roumina, R.; Mahmudi, R. Hot deformation of the extruded mg–10li–1zn alloy: Constitutive analysis and processing maps. *J. Alloys Compd.* **2017**, *696*, 1269–1277. [CrossRef]
37. Prasad, Y.V.R.K.; Seshacharyulu, T. Modelling of hot deformation for microstructural control. *Int. Mater. Rev.* **1998**, *43*, 243–258. [CrossRef]
38. Prasad, Y.V.R.K.; Sasidhara, S.; Sikka, V.K. Characterization of mechanisms of hot deformation of as-cast nickel aluminide alloy. *Intermetallics* **2000**, *8*, 987–995. [CrossRef]
39. Murty, S.V.S.N.; Rao, B.N. Instability map for hot working of 6061 al-10 vol% metal matrix composite. *J. Phys. D Appl. Phys.* **1998**, *31*, 3306. [CrossRef]
40. Poliak, E.I.; Jonas, J.J. A one-parameter approach to determining the critical conditions for the initiation of dynamic recrystallization. *Acta Mater.* **1996**, *44*, 127–136. [CrossRef]
41. Han, Y.; Liu, G.W.; Zou, D.N.; Sun, J.P.; Qiao, G.J. Investigation on hot deformation of 20Cr–25Ni superaustenitic stainless steel with starting columnar dendritic microstructure based on kinetic analysis and processing map. *Mater. Sci. Technol.* **2013**, *29*, 300–3008. [CrossRef]

Disclaimer/Publisher's Note: The statements, opinions and data contained in all publications are solely those of the individual author(s) and contributor(s) and not of MDPI and/or the editor(s). MDPI and/or the editor(s) disclaim responsibility for any injury to people or property resulting from any ideas, methods, instructions or products referred to in the content.